1 Regional study of mode-2 internal solitary waves in the Pacific coast
2 of Central America using marine seismic survey data

3 Wenhao Fan[1], Haibin Song[1], Yi Gong[1], Shun Yang[1], Kun Zhang[1]

4 [1] State Key laboratory of Marine Geology, School of Ocean and Earth Science, Tongji University, Shanghai, 200092, China

5 *Correspondence to*: Haibin Song (hbsong@tongji.edu.cn)

6 **Abstract.** In this paper, a regional study of the mode-2 internal solitary waves (ISWs) in the Pacific coast of Central
7 America is carried out by using seismic reflection method. The observed relationship between the dimensionless phase
8 velocity and the dimensionless amplitude (DA) of the mode-2 ISWs was analysed. When DA<1, the dimensionless phase
9 velocity increases with the increasing dimensionless amplitude, divided into two parts with different growth rates. When
10 DA>1, the dimensionless phase velocity increases with the increasing dimensionless amplitude at a relatively small growth
11 rate. We suggest that the influences of seawater depth (submarine topography), pycnocline depth, and pycnocline thickness
12 on the phase velocity of the mode-2 ISWs in the study area, cause the relationship between the dimensionless phase velocity
13 and the dimensionless amplitude diversified. The observed relationship between the dimensionless wavelength and the
14 dimensionless amplitude of the mode-2 ISWs was also analysed. When DA<1 and DA>2, the dimensionless wavelength
15 decreases and increases with the increasing dimensionless amplitude, respectively. Additionally, the seawater depth has a
16 great influence on the wavelength of the mode-2 ISWs in the study area, and overall the wavelength increases with the
17 increasing seawater depth. As for the vertical structure of the amplitude of the mode-2 ISWs in the study area, we find that it
18 is affected by the nonlinearity of the ISWs and the pycnocline deviation (especially the downward pycnocline deviation).

19 1 Introduction

20   The amplitude and propagation velocity of the mode-1 ISWs are larger than those in the mode-2 ISWs. The mode-1
21 ISWs are more common in the ocean. In recent years, with the advancement of observation instruments, the mode-2 ISWs in
22 the ocean have been gradually observed, such as on the New Jersey shelf (Shroyer et al., 2010), in the South China Sea (Liu
23 et al., 2013; Ramp et al., 2015; Yang et al., 2009), at Georges Bank (Bogucki et al., 2005), over Mascarene Ridge in Indian
24 Ocean (Da Silva et al., 2011)), and on the Australian North West Shelf (Rayson et al., 2019). Conventional physical
25 oceanography observation and remote sensing observation have spatial resolution limitations. That is, the horizontal
26 resolution of conventional physical oceanography observation methods (such as mooring) is low, and the vertical resolution
27 of remote sensing observations is low. Seismic oceanography (Holbrook et al., 2003; Ruddick et al., 2009), as a new
28 oceanography survey method, has high spatial resolution (the vertical resolution and horizontal resolution can reach about
29 10m). It can better describe the spatial structure and related characteristics of mesoscale and small scale phenomena in the

30 ocean (Biescas et al., 2008, 2010; Fer et al., 2010; Holbrook & Fer, 2005; Holbrook et al., 2013; Pinheiro et al., 2010;

31 Sallares et al., 2016; Sheen et al., 2009; Tsuji et al., 2005). Scholars have used seismic oceanography method to carry out

32 related studies on the geometry and kinematics characteristics of ISWs in the South China Sea, the Mediterranean Sea and

33 the Pacific Coast of Central America (Bai et al., 2017; Fan et al., 2021a, 2021b; Geng et al., 2019; Sun et al., 2019; Tang et

34 al., 2014, 2018).

35   At present, the researches on the mode-2 ISWs in the ocean are mainly based on simulation. Through simulation,

36 scholars have found that the pycnocline deviation will affect the stability of the mode-2 ISWs, making the top and bottom

37 structure of the mode-2 ISWs asymmetrical (Carr et al., 2015; Cheng et al., 2018; Olsthoorn et al., 2013). The instability

38 caused by the pycnocline deviation mainly appears at the bottom of the mode-2 ISWs, is manifested in that the amplitude of

39 the mode-2 ISWs peak is smaller than the amplitude of the trough, because the upper sea layer is thinner than the bottom sea

40 layer. The wave tail will appear similar to K-H instability billow and the wave core will appear small-scale flip (Carr et al.,

41 2015; Cheng et al., 2018). For the phase velocity of the mode-2 ISWs, scholars found through simulation experiments that it

42 increases with the increasing amplitude (Maxworthy, 1983; Salloum et al ., 2012; Stamp & Jacka, 1995; Terez & Knio,

43 1998). Brandt et al. (2014) simulated the material transport of mode-2 ISWs with large amplitude in the laboratory. They

44 found that, when $2a/h_2>4$ (a is the amplitude of the mode-2 ISWs and h_2 is the pycnocline thickness), the linear relationship

45 between the phase velocity (wavelength) and the amplitude is destroyed. That is, when the amplitude $2a/h_2\geq4$, the phase

46 velocity increases relatively slowly, and the wavelength increases rapidly. They believe that the above results are caused by

47 strong internal circulation related to the very large amplitude and the influence of the top and bottom boundaries. Chen et al.

48 (2014) calculated the KdV phase velocity and the fully nonlinear phase velocity of the ISWs as the function of the

49 pycnocline depth and the pycnocline thickness, respectively. They found the phase velocity of the mode-2 ISWs increases

50 monotonously with the increasing pycnocline depth, and firstly increases and then decreases with the increasing pycnocline

51 thickness. Carr et al. (2015) found by simulations that the pycnocline deviation has little effect on the phase velocity,

52 wavelength, and amplitude of the mode-2 ISWs. Maderich et al. (2015) found that for the mode-2 ISWs, when the

53 dimensionless amplitude $2a/h_2<1$, the deep water weakly nonlinear theory (Benjamin, 1967) can describe the numerical

54 simulation and experimental simulation results well. When $2a/h_2>1$, the wavelength (phase velocity) increases with the

55 amplitude faster than the results predicted by the deep water weakly nonlinear theory. But the solution of Kozlov and

56 Makarov (1990) can well estimate the corresponding wavelength and phase velocity when the amplitude is $1<2a/h_2<5$.

57 Terletska et al. (2016) found that the phase velocity and amplitude of the mode-2 ISWs will decrease after passing the step.

58 And the closer the mode-2 ISWs is to the step in the vertical direction at the time of incidence, the smaller the phase velocity

59 and amplitude of the mode-2 ISWs after passing the step. Kurkina et al. (2017) used GDEM (Generalized Digital

60 Environmental Model) to find that the seawater depth in the South China Sea is the main controlling factor of the mode-2

61 ISWs phase velocity, and the phase velocity increases exponentially with the increasing seawater depth. Deepwell et al.

62 (2019) found by simulation that the relationship curve that the mode-2 ISWs phase velocity increases with the increasing

63 amplitude has a strong quadratic fitting relationship. They speculated that this quadratic fitting relationship comes from the

64 influence of seawater depth (when the seawater depth is smaller, the phase velocity is also smaller).

65   The simulation can well reveal the kinematics characteristics of the mode-2 ISWs, but the actual ocean conditions are

66 often more complicated, which is manifested by the diversity of controlling factors in the kinematics process. The

67 observations including seismic oceanography method are also required to continually provide basic understanding of the

68 geometry and kinematics characteristics of the mode-2 ISWs. For example, limited by factors such as the lower spatial

69 resolution of the observation methods, previous scholars have less direct observation research on the phase velocity and

70 wavelength of the mode-2 ISWs in the ocean. And there is even less research (including observation research) on the vertical

71 structure of the mode-2 ISWs. The seismic oceanography method has more advantages for carrying out the above-mentioned

72 research due to its higher spatial resolution. The Pacific coast of Central America (western Nicaragua) has relatively

73 continuous submarine topography along the coastline, including continental shelf and continental slope, with the seawater

74 depth of 100-2000m (Fig. 1). At present, there is relatively little research work on internal waves in this area. We

75 reprocessed the historical seismic data in this area and identified a large number of mode-2 ISWs with relatively complete

76 spatial structures in the region. This discovery is very helpful to carry out observation research on the geometry and

77 kinematics characteristics of the mode-2 ISWs. Fan et al. (2021a, 2021b) used the multichannel seismic data of the survey

78 lines L88 and L76 (cruise EW0412, see Fig. 1 for the survey line locations) in the Pacific coast of Central America to

79 respectively report the mode-2 ISWs in this area and study the shoaling features of the mode-2 ISWs in this area. However, a

80 single survey line can only reveal the local characteristics of the mode-2 ISWs in the study area. Deep understanding of the

81 geometry and kinematics characteristics of the mode-2 ISWs in the study area requires a regional systematic study. In this

82 work, we reprocessed the seismic data of the entire study area, and identified numerous mode-2 ISWs on multiple survey

83 lines in the region (the positions of the observed ISWs and the survey lines they located are shown by the black filled circles

84 and the red lines in Fig. 1, respectively). Based on the numerous mode-2 ISWs observed by multiple survey lines in the study

85 area, this paper will conduct a regional study on the characteristic parameters such as the pycnocline deviation degree, phase

86 velocity, and wavelength of the mode-2 ISWs, as well as the vertical structure characteristics of the mode-2 ISWs' amplitude

87 in the study area.

88
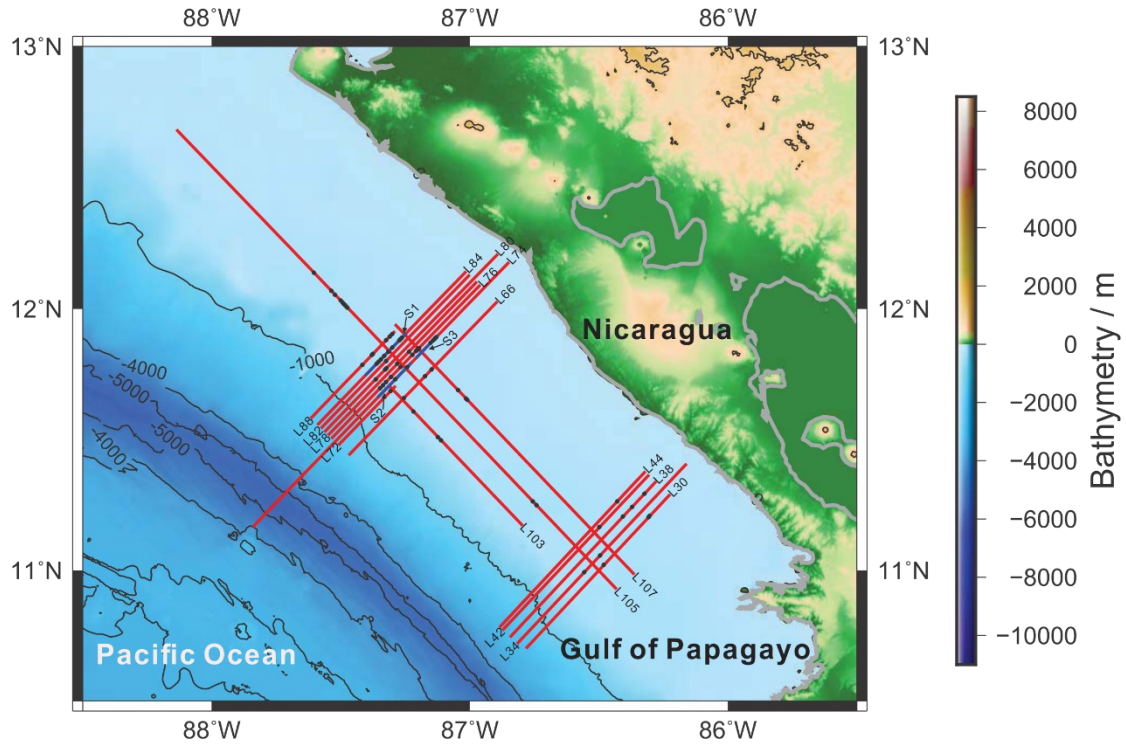
Figure 1. Distribution of multichannel seismic data. The red lines indicate the positions of the survey lines, and the black filled circles on the red lines indicate the positions of the observed mode-2 ISWs. The blue lines S1, S2 and S3 are part of the seismic sections containing the mode-2 ISWs, which will be displayed in Fig. 3 and Fig. 4.

2 Data and Methods

This paper mainly uses seismic reflection to conduct a regional study on the mode-2 ISWs in the Pacific coast of Central America. The seismic data of the cruise EW0412 used in this study was provided by the MGDS (The Marine Geoscience Data System) (http://www.marine-geo.org/). The cruise EW0412 collected high-resolution multichannel seismic data from the continental shelf to the continental slope in the coastal areas of Sandino Forearc Basin, Costa Rica, Nicaragua, Honduras, and El Salvador (Fulthorpe & McIntosh, 2014). The seismic acquisition parameters of the cruise EW0412 are as follows: the sampling interval is 1 ms, each shot gather has 168 traces, the shot interval is 12.5 m, the trace interval is 12.5 m, and the minimum offset is 16.65 m. The seawater seismic reflection sections used in this study were obtained through the following processing processes: defining geometry, noise attenuation, common midpoint (CMP) sorting, velocity analysis, normal moveout (NMO), stacking, and post-stack denoising.

The mode-2 ISWs in the actual ocean has the multilayer structure, which is different from the three-layer model used in the simulation experiment to describe the convex mode-2 ISWs. As for three-layer model, the upper layer of the convex mode-2 ISWs is the peak and the lower layer is the trough. In order to establish the connection between this observational data research and previous simulation experiments, we calculated the equivalent amplitude, the equivalent pycnocline

107 thickness, and the equivalent wavelength of the mode-2 ISWs. For the mode-2 ISWs with a multilayer structure, the sum of

108 all ISWs peak amplitudes a_p and the sum of all ISWs trough amplitudes a_t are respectively taken as the equivalent peak and

109 trough amplitude of the mode-2 ISWs with a three-layer model structure. Then the equivalent amplitude of the mode-2 ISWs

110 with a three-layer model structure is the average of a_p and a_t, and the equivalent pycnocline thickness is calculated by $h_2=h-$

111 a_p-a_t, where h is the seawater thickness affected by the mode-2 ISWs with a multilayer structure. The equivalent wavelength

112 of the mode-2 ISWs with a three-layer model structure is the average of all ISWs peak and trough wavelengths in the

113 multilayer structure. The detailed calculation process is described in Fan et al. (2021a). This study uses an improved ISWs

114 apparent phase velocity calculation method to calculate the apparent phase velocity of ISWs. This method firstly does pre-

115 stack migration of the common offset gather sections, and then pick the CMP and shot point pairs corresponding to the ISWs

116 trough or peak from the pre-stack migration sections of different offset with high signal-to-noise ratio. By fitting the CMP-

117 shot point pairs, we can calculate the apparent phase velocity and apparent propagation direction of the ISWs. The ISWs

118 horizontal velocity can be expressed by $v=(cmp2-cmp1)/T=(cmp2-cmp1)/[(s2-s1)*dt]$, where $cmp1$ and $cmp2$ are the peak or

119 trough positions of the ISWs at different time, $s1$ and $s2$ are the shot numbers corresponding to $cmp1$ and $cmp2$, and dt is the

120 time interval of shots. The detailed calculation process is described in Fan et al. (2021a).

121   The wavelength of the mode-2 ISWs is usually defined as half-width at half-amplitude of the ISWs (Carr et al., 2015;

122 Stamp & Jacka, 1995), as shown by λ in Fig. 2. Since the ISWs move in the horizontal direction during the seismic

123 acquisition process, the wavelength of the ISWs observed by the seismic reflection method is the apparent wavelength. The

124 apparent wavelength of the ISWs is controlled by the relative motion direction of the ship and the ISWs, the ship speed, and

125 the propagation speed of the ISWs. The propagation speed of the mode-2 ISWs (about 0.5m/s) is generally lower than the

126 ship speed (about 2.5m/s) during seismic acquisition. When correcting the apparent wavelength of the ISWs to obtain the

127 actual wavelength, it is divided into two situations in which the motion direction of the ISWs and the ship is the same and

128 opposite, as shown in Fig. 2. When the ISWs and the ship move in the same direction, the wavelength (apparent wavelength)

129 estimated from the seismic stacked section is larger. That is, the wavelength (apparent wavelength λ_s) of the ISWs observed

130 on the seismic stacked section denoted by the blue curve in Fig. 2a is greater than the wavelength λ of the actual ISWs at the

131 beginning and end respectively denoted by the black and red curves in Fig. 2a. In order to eliminate the influence of the

132 horizontal movement of the ISWs, when correcting the apparent wavelength λ_s to obtain the actual wavelength λ, it is

133 necessary to subtract the distance x_w moved by the ISWs within the seismic acquisition time corresponding to the apparent

134 wavelength distance of the ISWs. That is:

135 $$\lambda = \lambda_s - x_w = \lambda_s - \lambda_s/V_{ship} * V_{water} \qquad (1)$$

136 where V_{ship} is the ship speed, and V_{water} is the propagation speed of the ISWs (Fig. 2a).

137   When the ISWs and the ship move in the opposite direction, the wavelength (apparent wavelength) estimated from the

138 seismic stacked section is smaller. That is, the wavelength (apparent wavelength λ_s) of the ISWs observed on the seismic

139 stacked section denoted by the blue curve in Fig. 2b is smaller than the wavelength λ of the actual ISWs at the beginning and

140 end respectively denoted by the black and red curves in Fig. 2b. In order to eliminate the influence of the horizontal

141 movement of the ISWs, when correcting the apparent wavelength λ_s to obtain the actual wavelength λ, it is necessary to add

142 the distance x_w moved by the ISWs within the seismic acquisition time corresponding to the apparent wavelength distance of

143 the ISWs. That is:

144 $$\lambda = \lambda_s + x_w = \lambda_s + \lambda_s/V_{ship} * V_{water} \qquad (2)$$

145 where V_{ship} is the ship speed, and V_{water} is the propagation speed of the ISWs (Fig. 2b).

146

(a)   (b)
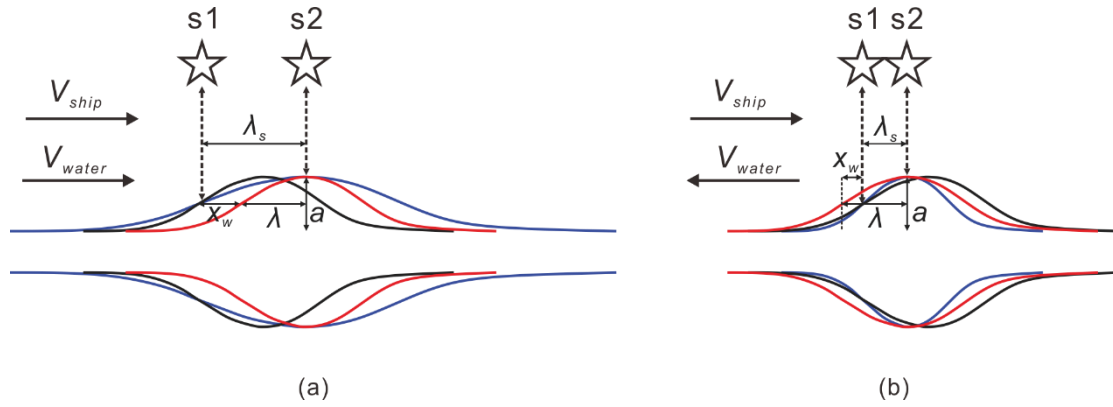
148 **Figure 2. Schematic diagram of the apparent wavelength correction of the mode-2 ISWs. (a) The ISWs move in the same direction**
149 **as the ship. (b) The ISWs move in the opposite direction to the ship. S1 denotes the self-excitation and self-reception position of the**
150 **ship at 1/2 amplitude of the ISWs at the beginning. S2 denotes the self-excitation and self-reception position of the ship at the peak**
151 **of the amplitude of the ISWs. V_{ship} is the ship speed, and V_{water} is the ISWs propagation speed. λ_s is the apparent wavelength of the**
152 **ISWs observed by the seismic stacked section. λ is the actual wavelength of the ISWs. a is the amplitude of the ISWs. x_w is the**
153 **distance moved by the ISWs during the time the ship moves from S1 to S2. The black curve denotes the ISWs at the beginning, the**
154 **red curve denotes the ISWs moved x_w distance from the starting position, and the blue curve denotes the ISWs observed on the**
155 **seismic stacked section.**

156 **3 Results and Interpretations**

157 **3.1 Typical Sections Interpretation and Regional Distribution Characteristics of the Mode-2 ISWs**

158   In addition to the survey lines L88 and L76 with mode-2 ISWs observed by Fan et al. (2021a, 2021b), we also found

159 mode-2 ISWs on many other survey lines in the study area. Two typical survey lines are L84 and L74 (see the red lines in

160 Fig. 1 for the locations of these two survey lines). Figure 3 shows the partial seismic stacked section S1 of the survey line

161 L84 (see the blue line in Fig. 1 for the location of this section S1). We have identified 10 mode-2 ISWs from the seismic

162 section S1 (see Fig. 3 for their positions and corresponding numbers. ISW1-ISW4 are located at the shelf break, and ISW5-

163 ISW10 are located on the continental shelf), and calculated the characteristic parameters of these 10 mode-2 ISWs, such as

164 the seafloor depth (seawater depth) H, maximum amplitude (in the vertical direction), equivalent amplitude a, equivalent

165 pycnocline thickness h_2, dimensionless amplitude $2a/h_2$, mid-depths of the pycnocline hc , the degree to which the mid-depth

166 of the pycnocline deviates from 1/2 seafloor depth Op, equivalent wavelength λ, dimensionless wavelength $2\lambda/h_2$, and

167 apparent phase velocity U_c (Table 1). The equivalent wavelength and the dimensionless wavelength in Table 1 have been

168 corrected using Eq. (1) (the ISWs have the same motion direction as the ship, and the ISWs with the large phase velocity

169 estimation error have been corrected using a phase velocity of 0.5m/s). The maximum amplitudes of the ISWs ISW1-ISW7

170 on the survey line L84 are all less than 10m, and the maximum amplitudes of ISW8-ISW10 are larger, around 15m. The

171 $2a/h_2$ values of these ten mode-2 ISWs on the survey line L84 are all less than 2, and they belong to the mode-2 ISWs with

172 small amplitude (Brandt et al., 2014). The $2a/h_2$ values of ISW8, ISW9, and ISW10 are around 1, and their amplitudes are

173 slightly larger in these small-amplitude mode-2 ISWs. When calculating the degree to which the mid-depth of the pycnocline

174 deviates from 1/2 seafloor depth, it is found that except for the pycnocline centres of ISW8, ISW9, and ISW10 are deeper

175 than 1/2 seafloor depths, the pycnocline centres of the other seven mode-2 ISWs are shallower than 1/2 seafloor depths. For

176 ISW1, ISW2, and ISW3, the degrees to which the mid-depth of the pycnocline deviates from 1/2 seafloor depth are both

177 greater than 20%, which appear as the asymmetry of waveforms (the asymmetry of the front and rear waveform, and the

178 asymmetry of the top and bottom waveform). When the degree to which the mid-depth of the pycnocline deviates from 1/2

179 seafloor depth is small, the waveform of the mode-2 ISWs is more symmetrical, such as ISW8, ISW9, and ISW10. The

180 waveforms of ISW1, ISW2, and ISW3 at the shelf break are asymmetrical, and their dimensionless wavelength $2\lambda/h_2$ is

181 significantly larger than the $2\lambda/h_2$ of the ISWs on the continental shelf which have the same level of dimensionless

182 amplitudes ($2a/h_2$) (for example, the $2a/h_2$ value of ISW2 is 0.45, and the value of $2\lambda/h_2$ is 9.55; the value of $2a/h_2$ of ISW7 is

183 0.42, and the value of $2\lambda/h_2$ is 3.49), making the overall relationship between dimensionless wavelength $2\lambda/h_2$ and the

184 dimensionless amplitude $2a/h_2$ are not absolute linear correlation (the dimensionless wavelength $2\lambda/h_2$ increases with the

185 increasing dimensionless amplitude). The apparent phase velocities of the 10 mode-2 ISWs on the survey line L84 are about

186 0.5 m/s, and the apparent propagation directions are all shoreward. For ISWs with small apparent phase velocity calculation

187 errors in shallow water (ISW6, ISW7, and ISW9), the apparent phase velocity does not strictly increase with the increasing

188 dimensionless amplitude $2a/h_2$. For example, the $2a/h_2$ value of ISW6 is 0.4 , and the apparent phase velocity is about 0.58

189 m/s; The $2a/h_2$ value of ISW9 is 1.19, and the apparent phase velocity is about 0.38 m/s.

190
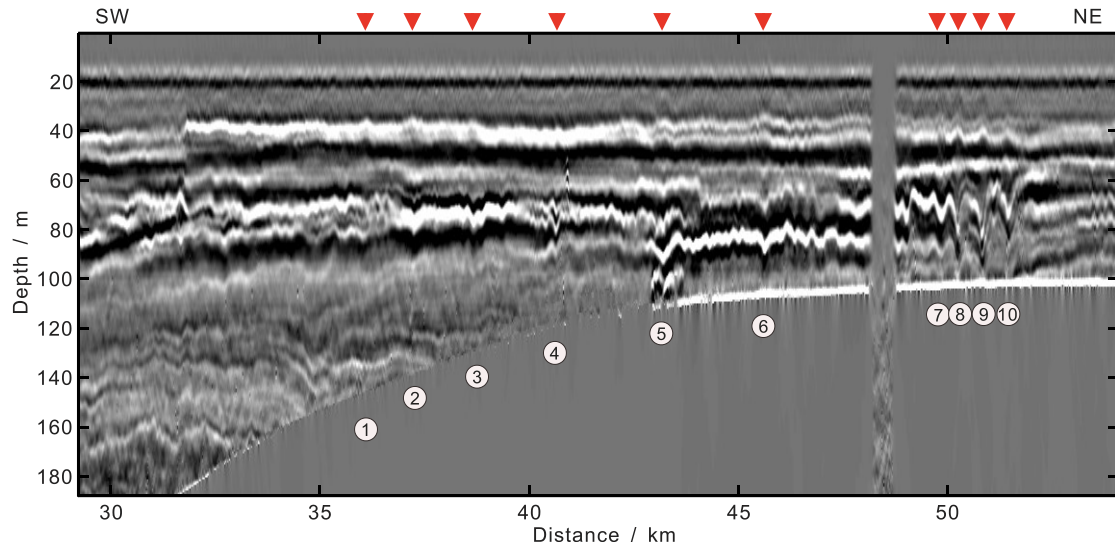
Figure 3. Seismic stacked section S1, observed mode-2 ISWs part on the survey line L84. Arrows and numbers indicate the ten identified mode-2 ISWs ISW1-ISW10. The location of the S1 seismic stacked section is shown in Fig. 1. The horizontal axis indicates the distance to the starting point of the survey line L84. The survey line L84 acquisition time is from 07:15:14 on 17 December 2004, to 17:26:49 on 17 December 2004.

Table 1. Characteristic Parameters of the 10 Mode-2 Internal Solitary Waves in Survey Line L84.

ISW#	H (m)	A (m)	a (m)	h_2 (m)	$2a/h_2$	hc (m)	Op (%H)	λ (m)	$2\lambda/h_2$	U_c (m/s)
ISW1	145.5	3	2.22	29.23	0.15	54.88	24.6	103.6	7.09	0.85±0.6
ISW2	138.8	4.7	5.84	25.93	0.45	51.31	26.1	123.8	9.55	0.69±0.19
ISW3	130.5	4.1	4.45	27.6	0.32	49.05	24.8	84.6	6.13	0.52±0.12
ISW4	121.5	5.2	6.04	34.72	0.35	59.4	2.2	55.18	3.18	0.19±0.11
ISW5	111	6.79	12.67	40.84	0.62	51.31	7.6	95.38	4.67	0.32±0.16
ISW6	108	4.6	7.5	37.19	0.4	48.48	10.2	50.61	2.72	0.58±0.16
ISW7	104.3	6.4	7.34	34.83	0.42	48.11	7.8	60.86	3.49	0.64±0.28
ISW8	103.5	13.2	15.82	32.94	0.96	53.38	-3.2	72.97	4.43	0.46±0.24
ISW9	103.5	15.9	13.56	22.79	1.19	52.81	-2.1	88.47	7.76	0.38±0.17
ISW10	102.8	13.6	15.87	20.62	1.54	52.62	-2.4	94.1	9.13	0.55±0.34

Note. H, seafloor depths. A, maximum amplitudes. a, equivalent ISWs amplitudes. h_2, equivalent pycnocline thicknesses. hc, the mid-depths of the pycnocline. Op, the degree to which the mid-depth of the pycnocline deviates from 1/2 seafloor depth. λ, equivalent wavelengths. U_c, apparent phase velocities obtained from seismic observation.

202

203   The survey line L74 is located in the southeast direction of the survey line L84 (see Fig. 1 for the specific location).
204 Figure 4 shows the partial seismic stacked sections (S2 and S3) of the survey line L74. We have identified seven mode-2
205 ISWs from the seismic sections S2 and S3. Their positions and corresponding numbers are shown in Fig. 4, and the
206 statistical characteristic parameters are shown in Table 2. The equivalent wavelength and the dimensionless wavelength in
207 Table 2 have been corrected using Eq. (1) (the ISWs have the same motion direction as the ship, and the ISWs with the large
208 phase velocity estimation error have been corrected using a phase velocity of 0.5 m/s). The maximum amplitudes of the
209 ISWs ISW12-ISW17 on the survey line L74 are all less than 10 m, and the maximum amplitude of ISW11 is larger, 13.6 m.
210 The $2a/h_2$ values of these seven mode-2 ISWs are all less than 2. They are the mode-2 ISWs with small amplitude , and the
211 amplitude of ISW11 is slightly larger among them. When calculating the degree to which the mid-depth of the pycnocline
212 deviates from 1/2 seafloor depth, it is found that the pycnocline centres of the mode-2 ISWs ISW11-ISW17 are all deeper
213 than 1/2 of the seafloor depths. Except for ISW11 (the bottom reflection event is broken), as for the other six mode-2 ISWs
214 ISW12-ISW17, the degrees to which the mid-depth of the pycnocline deviates from 1/2 seafloor depth are both greater than
215 15%. The asymmetry of ISW12 and ISW13 is manifested in that the connection between the top peaks of the ISWs and the
216 bottom troughs of the ISWs is not vertical. The pycnocline centre of ISW14 deviates from 1/2 of the seafloor depth the most,
217 which is 51.5%. Its asymmetry is manifested in the large difference between the top and bottom waveforms near the
218 pycnocline centre. ISW15, ISW16, and ISW17 are located on the continental shelf, and their pycnocline deviations are larger,
219 but the waveforms are more symmetrical than other ISWs. When the downward pycnocline deviation is large, the influence
220 of pycnocline deviation on the stability of the mode-2 ISWs is more complicated than when the pycnocline deviates upwards,
221 and it may be controlled by factors such as wavelength. There is no absolute linear correlation relationship between the
222 dimensionless wavelength $2\lambda/h_2$ and the dimensionless amplitude $2a/h_2$ of the seven mode-2 ISWs on the survey line L74
223 (the dimensionless wavelength $2\lambda/h_2$ increases with the increasing dimensionless amplitude $2a/h_2$). For example, the $2a/h_2$
224 values of ISW12 and ISW14 are greater than that of ISW16, but the dimensionless wavelength of ISW16 is greater than the
225 dimensionless wavelengths of ISW12 and ISW14. The apparent phase velocities of the seven mode-2 ISWs on the survey
226 line L74 are about 0.5 m/s, and their propagation directions are all shoreward. For the ISWs in shallow water where the
227 apparent phase velocity calculation errors are small (ISW12, ISW14, ISW16, and ISW17), the apparent phase velocity
228 generally increases with the increasing dimensionless amplitude $2a/h_2$.

229

230
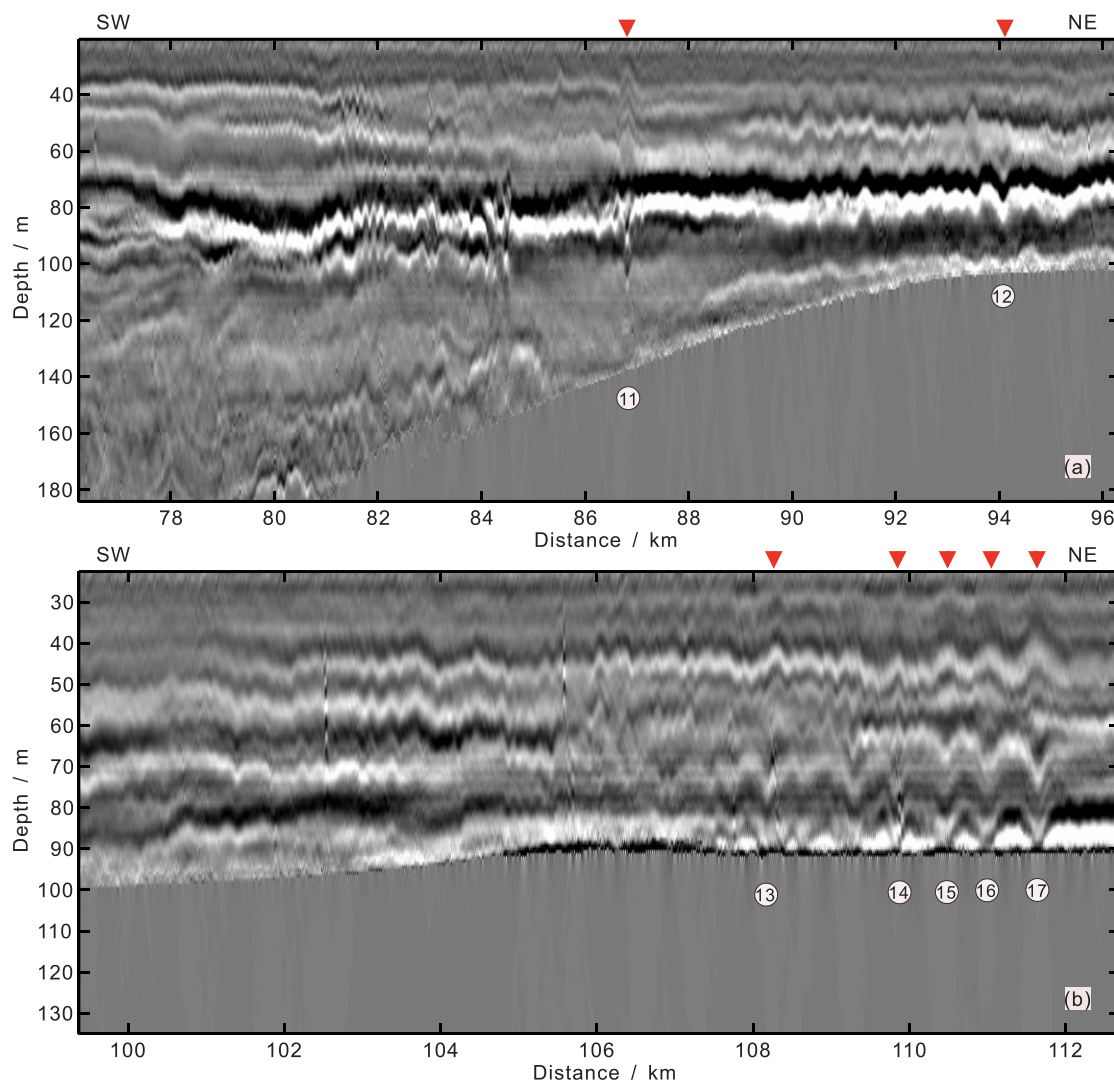
Figure 4. (a) and (b) are respectively the seismic stacked sections S2 and S3, observed mode-2 ISWs parts on the survey line L74.
The arrows and the numbers indicate the seven identified mode-2 ISWs ISW11-ISW17. The locations of the seismic stack section
S2 and S3 are shown in Fig. 1, and the horizontal axis indicates the distance to the starting point of the survey line L74. The survey
line 74 acquisition time is from 06:31:03 on 3 December 2004 to 02:30:01 on 4 December 2004.

235

236 **Table 2. Characteristic Parameters of the Seven Mode-2 Internal Solitary Waves in Survey Line L74.**

ISW#	H (m)	A (m)	a (m)	h_2 (m)	$2a/h_2$	hc (m)	Op (%H)	λ (m)	$2\lambda/h_2$	U_c (m/s)
ISW11	138.8	13.6	24.19	26.98	1.79	73.38	-5.7	83.05	6.16	0.19±0.1
ISW12	103.5	7.31	9.95	32.82	0.61	60.34	-16.6	68.11	4.15	0.63±0.08

ISW13	90.75	5.68	6.08	36.22	0.34	55.62	-22.6	94.41	5.21	0.49±0.24
ISW14	92.25	6.86	11.17	35.04	0.64	68.35	-51.5	50.69	2.89	0.49±0.21
ISW15	90	5.46	8.91	38.94	0.46	52.1	-15.8	112.7	5.79	0.36±0.26
ISW16	91.5	5.74	8.67	39.53	0.44	57.97	-26.7	100.7	5.09	0.60±0.17
ISW17	91.5	6.4	12.71	32.56	0.78	57.6	-25.9	69.56	4.27	1.07±0.2

237 **Note. H, seafloor depths. A, maximum amplitudes. a, equivalent ISWs amplitudes. h_2, equivalent pycnocline thicknesses. hc, the**
238 **mid-depths of the pycnocline. Op, the degree to which the mid-depth of the pycnocline deviates from 1/2 seafloor depth. λ,**
239 **equivalent wavelengths. U_c, apparent phase velocities obtained from seismic observation.**

240

241   In addition to the survey lines L74 and L84, the mode-2 ISWs also have sporadic distribution on other survey lines in
242 the area (see the black filled circles in Fig. 1). We have identified 70 mode-2 ISWs in the study area. They appeared from 2
243 December 2004 to 18 December 2004. On 17 December 2004 and 18 December 2004, there were more mode-2 ISWs (Fig.
244 5a), 21 (10 for survey line L84, 6 for survey line L88, and 5 for survey line L76) and 9 (1 for survey line L72, 5 for survey
245 line L76, and 3 for survey line L103) respectively. Observe the distribution of the appearance time of mode-2 ISWs observed
246 in the study area in Fig. 5a (in days). It can be found that the mode-2 ISWs frequently appeared on the northwest side of the
247 study area in December 2004, and appeared in early and late December. In addition, the spatial distribution range of the
248 mode-2 ISWs is large, ranging from the continental slope to the continental shelf (see Figures 1, 3, and 4). Figure 5b shows
249 the time when the mode-2 ISWs observed in the study area appeared in hours. Combined with Fig. 5a, it can be found that
250 from 2 December 2004 to 8 December 2004, the ISWs appeared at around 12:00 and 00:00 (or 24:00) in a day; From 10
251 December 2004 to 13 December 2004, the ISWs appeared at around 12:00 and 24:00 in a day, and relatively more appeared
252 around 12:00; From 14 December 2004 to 18 December 2004, the ISWs appeared at around 12:00 and 00:00 (or 24:00) in a
253 day, and relatively more appeared around 00:00 (or 24:00). The survey lines L103, L105, and L107 are perpendicular to the
254 propagation direction of the mode-2 ISWs in the study area (Fig. 1). Therefore, these three survey lines are not included in
255 the subsequent statistical analysis of the mode-2 ISWs characteristic parameters. We have counted the characteristic
256 parameters of 53 mode-2 ISWs in the study area. In these 53 mode-2 ISWs, there are 51 small-amplitude ISWs ($2a/h_2<2$),
257 and there are 40 ISWs with smaller amplitude ($2a/h_2<1$) among these 51 small-amplitude ISWs (Fig. 6a). The mode-2 ISWs
258 in the study area are dominated by smaller amplitudes (Fig. 6a). The maximum amplitude (in the vertical direction) of the
259 mode-2 ISWs mainly changes in the range of 3-13 m (Fig. 6d), and the equivalent wavelengths of most of the mode-2 ISWs
260 are on the order of about 100 m (Fig. 6c, the equivalent wavelength in the figure has been corrected according to Eq. (1) and
261 Eq. (2)). When calculating the phase velocity of the mode-2 ISWs, due to the low signal-to-noise ratio of some survey lines,
262 the calculation errors of some ISWs phase velocities are relatively large. Therefore, when analysing the apparent phase
263 velocity of the mode-2 ISWs of the study area, we only used 26 ISWs with relatively small errors (the error is less than half

264 of the calculated value). The apparent phase velocities of the mode-2 ISWs in the study area are on the order of 0.5 m/s (Fig.

265 6b), and most of the mode-2 ISWs propagate in the shoreward direction. We have traced back the time when each ISWs in

266 the study area (mainly the ISWs located on the continental shelf) appeared at the continental shelf break using the ISWs

267 phase velocity of 0.5 m/s, as shown in Fig. 5c, in hours. Combined with Fig. 5a, it is found that from 2 December 2004 to 8

268 December 2004, the ISWs traced back to the continental shelf break appeared at around 12:00 and 00:00 (or 24:00) in a day,

269 and relatively more appeared around 12:00; From 10 December 2004 to 13 December 2004, most of the ISWs traced back to

270 the continental shelf break appeared at around 24:00 (or 0:00) in a day; From 14 December 2004 to 18 December 2004, the

271 ISWs traced back to the continental shelf break appeared at around 12:00 and 24:00 (or 0:00) in a day. The mode-2 ISWs

272 observed in the study area may be generated by the interaction between the internal tide and the continental shelf break.

273

274
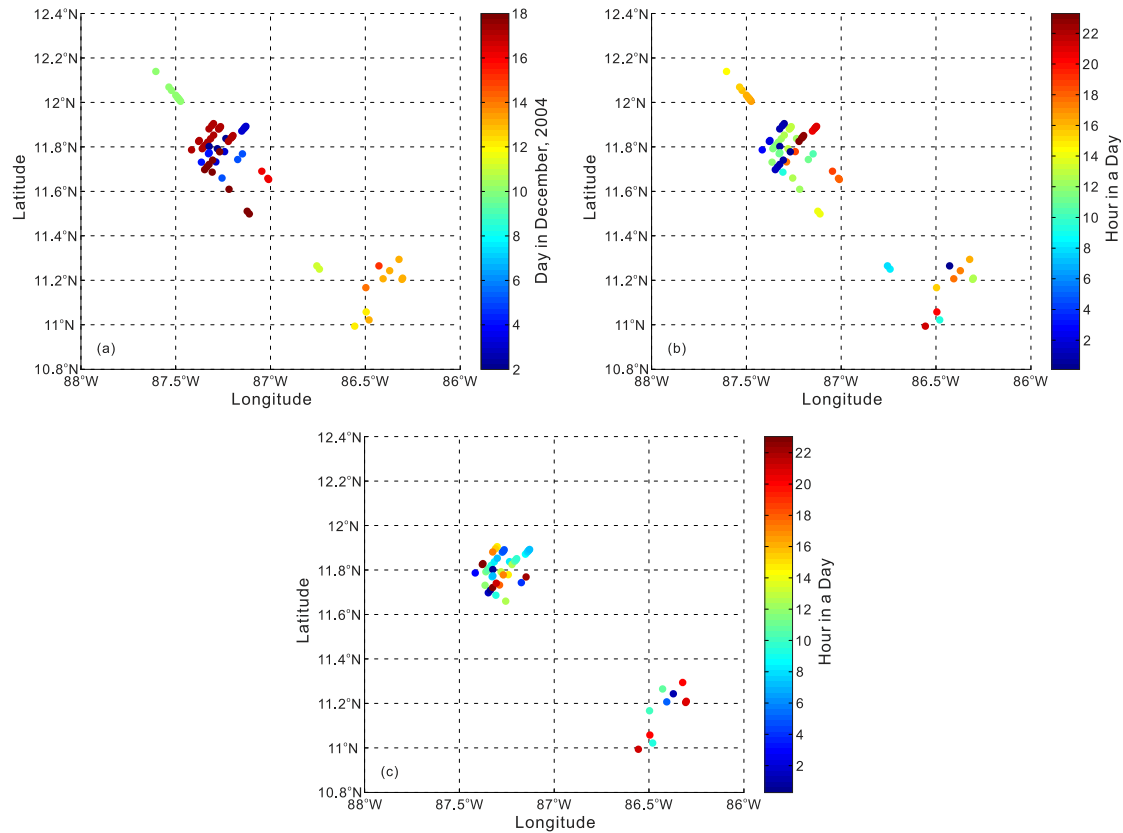
275 **Figure 5. (a) The time when the mode-2 ISWs observed in the study area appeared in days. (b) The time when the mode-2 ISWs**
276 **observed in the study area appeared in hours. (c) Tracing back the time (in hours) when internal solitary waves appeared at the**
277 **continental shelf break in the study area.**

278
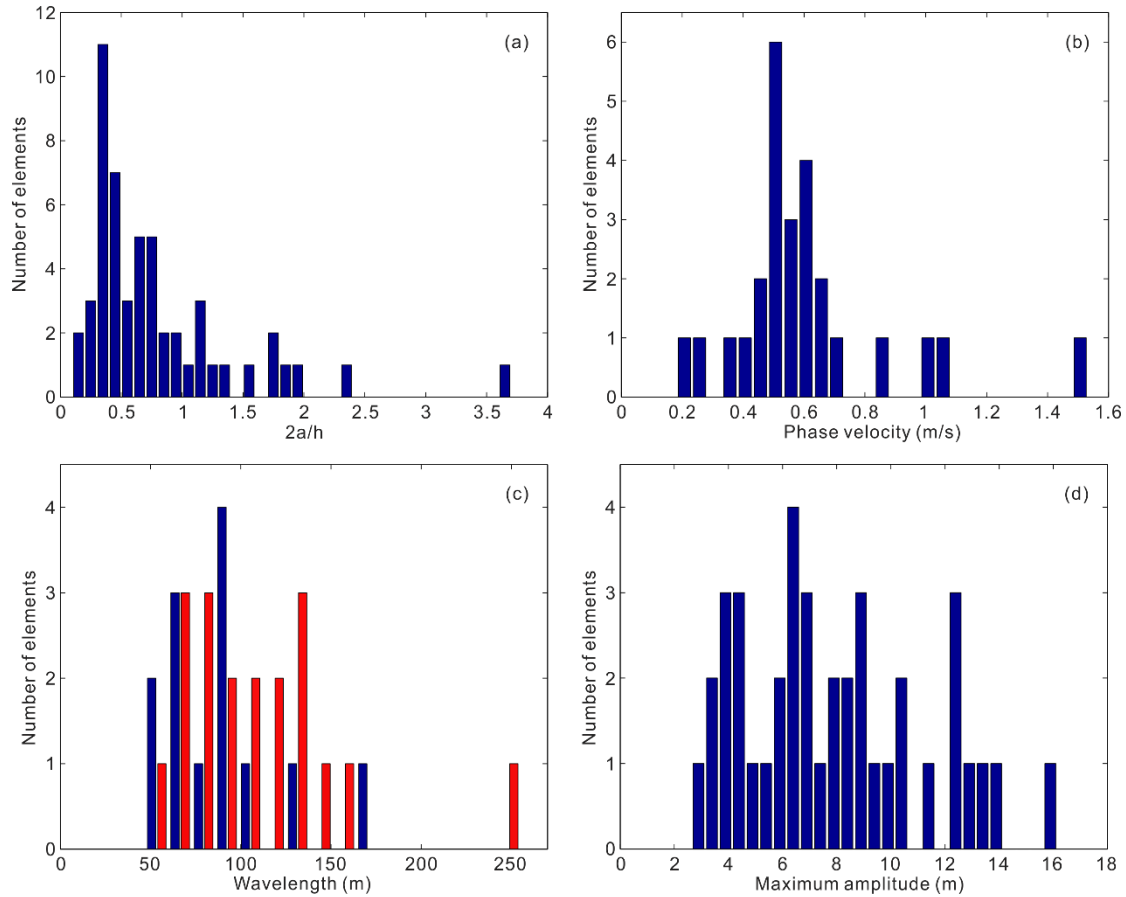
Figure 6. (a) The histogram of the dimensionless amplitude of the mode-2 ISWs in the study area. (b) The histogram of the phase velocity of the mode-2 ISWs in the study area. (c) The histogram of the wavelength of the mode-2 ISWs in the study area, the dark blue and red colour bars denote the ISWs on the survey lines in SW-NE direction and in NE-SW direction, respectively. (d) The histogram of the maximum amplitude of the mode-2 ISWs in the study area.

3.2 Phase Velocity and Wavelength Characteristics of the Mode-2 ISWs in Study Area

Inspired by the work of Maderich et al. (2015) and Chen et al. (2014), we respectively calculated the relationships between the dimensionless phase velocity and the dimensionless amplitude, the dimensionless wavelength and the dimensionless amplitude, the phase velocity (apparent phase velocity) and the maximum amplitude, the wavelength (equivalent wavelength) and the maximum amplitude, the phase velocity (apparent phase velocity) and the pycnocline depth, the phase velocity (apparent phase velocity) and the pycnocline thickness. Figure 7 shows the relationship between the dimensionless phase velocity U_c/C and the dimensionless amplitude $2a/h_2$ of the observed 26 mode-2 ISWs (with relatively small errors) in the study area. When $2a/h_2<1$, the relationship between the dimensionless phase velocity and the dimensionless amplitude of the observed mode-2 ISWs in the study area has the trends respectively given by Kozlov and

294   Makarov (1990), as well as Salloum et al. (2012). That is, the dimensionless phase velocity of the mode-2 ISWs increases
295   with the increasing dimensionless amplitude, but with different growth rates. When $2a/h_2 > 1$, the relationship between the
296   dimensionless phase velocity and the dimensionless amplitude of the observed mode-2 ISWs in the study area is closer to the
297   result predicted by the deep water weakly nonlinear theory (Benjamin, 1967). That is, The dimensionless phase velocity of
298   the mode-2 ISWs increases with the increasing dimensionless amplitude at a relatively small growth rate. Figure 8 shows the
299   relationship between the dimensionless wavelength $2\lambda/h_2$ and the dimensionless amplitude $2a/h_2$ of the observed 32 mode-2
300   ISWs (there are 13 ISWs on the survey lines in SW-NE direction, and 19 ISWs on the survey lines in NE-SW direction, see
301   Fig. 6c) in the study area, where the black and red crosses denote the ISWs on the survey lines in SW-NE direction and in
302   NE-SW direction, respectively. The survey line in SW-NE direction is consistent with the movement direction of the ISWs.
303   Use Eq. (1) to correct the apparent wavelength to obtain the actual wavelength. The survey line in NE-SW direction is
304   opposite to the movement direction of the ISWs. Use Eq. (2) to correct the apparent wavelength to obtain the actual
305   wavelength. Figure 8 shows the result after correcting the apparent wavelength of the ISWs. When using Eq. (1) and Eq. (2)
306   to correct the apparent wavelength, the phase velocity of the ISWs estimated in Fig. 7 needs to be used. The dimensionless
307   wavelengths of the ISWs with the large error in the estimation of the phase velocity are not shown in Fig. 8. Observing Fig. 8,
308   it can be found that when $2a/h_2 < 1$, the relationship between the dimensionless wavelength and the dimensionless amplitude
309   of the observed mode-2 ISWs in the study area is closer to the result predicted by the deep water weakly nonlinear theory
310   (Benjamin, 1967). That is, the dimensionless wavelength of the mode-2 ISWs decreases with the increasing dimensionless
311   amplitude. When $2a/h_2 > 2$, the relationship between the dimensionless wavelength and the dimensionless amplitude of the
312   observed mode-2 ISWs in the study area is closer to the solution of Salloum et al. (2012). That is, the dimensionless
313   wavelength of the mode-2 ISWs increases with the increasing dimensionless amplitude. When $1 < 2a/h_2 < 2$, the dimensionless
314   wavelength of the observed mode-2 ISWs in the study area is higher than that predicted by the deep water weakly nonlinear
315   theory (Benjamin, 1967) and Salloum et al. (2012).

316

317
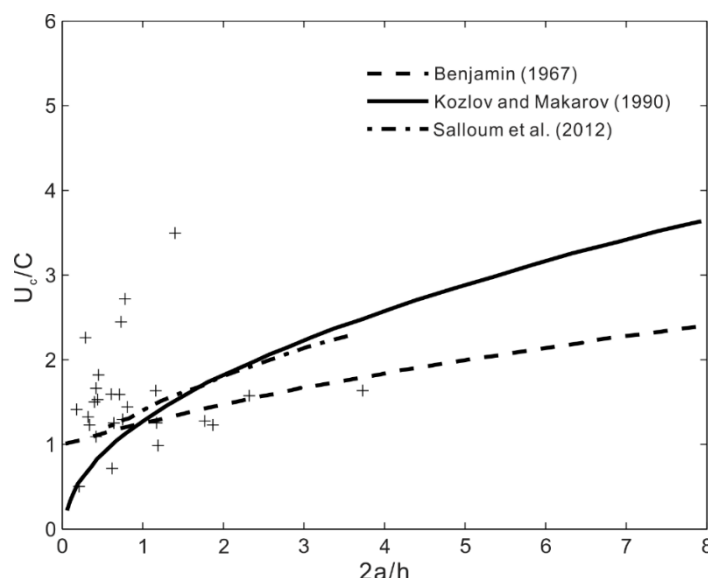
Figure 7. The relationship between the dimensionless phase velocity and the dimensionless amplitude of the mode-2 ISWs observed
in the study area. The black crosses denote the seismic observation results of the mode-2 ISWs.

320

321
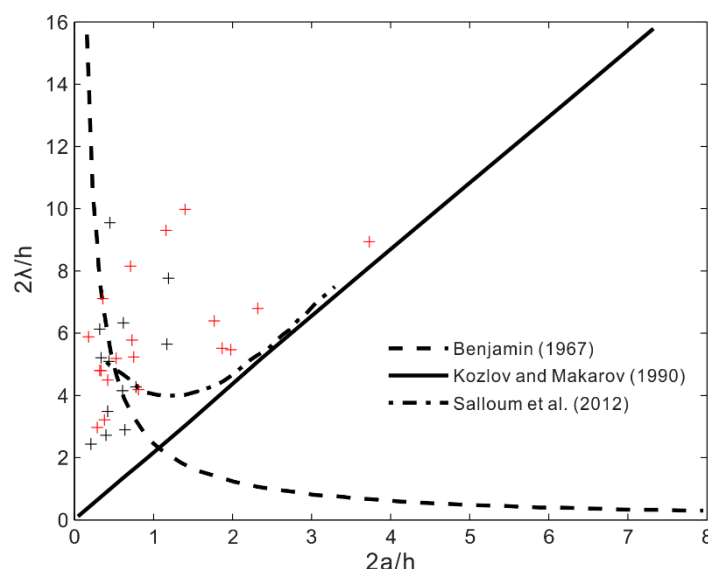
Figure 8. The relationship between the dimensionless wavelength and the dimensionless amplitude of the mode-2 ISWs observed in
the study area. The black and red crosses denote the ISWs on the survey lines in SW-NE direction and in NE-SW direction,
respectively.

325

326   The relationship between the phase velocity and the maximum amplitude of the mode-2 ISWs observed in the study

327   area, and the relationship between the wavelength and the maximum amplitude are shown in Figs. 9a and 9b, respectively. It

328   can be found that the phase velocity and wavelength of the mode-2 ISWs in the study area are less affected by the maximum

329 amplitude. There is no obvious linear correlation between phase velocity and maximum amplitude, as well as between
330 wavelength and maximum amplitude (Figs. 9a and 9b). When the maximum amplitudes are between 6 m and 11 m, the
331 variety range of phase velocity is relatively large, and there is a significant increase in phase velocity (Fig. 9a). When the
332 maximum amplitudes are between 7 m and 13 m, there is a significant increase in wavelength (Fig. 9b). The relationships
333 between the phase velocity and the pycnocline depth, as well as the phase velocity and the pycnocline thickness of the
334 observed mode-2 ISWs in the study area are shown in Figs. 10a and 10b, respectively. As for the observed mode-2 ISWs in
335 the study area, their pycnocline depths are mainly concentrated in the range of 40-70 m, and their pycnocline thicknesses
336 (equivalent pycnocline thickness) are mainly concentrated in the range of 10-60 m. As with the numerical simulation results
337 of Chen et al. (2014), the phase velocity of the observed mode-2 ISWs in the study area has the trends to increase slowly
338 with the increasing pycnocline depth and pycnocline thickness, respectively. The trend mentioned above is not completely
339 monotonous in Fig. 10, which is manifested as the large variation range of the phase velocity on the vertical axis. We analyse
340 it is caused by the fact that other factors (such as seawater depth), other than the pycnocline depth and the pycnocline
341 thickness, also affect the phase velocity.

342
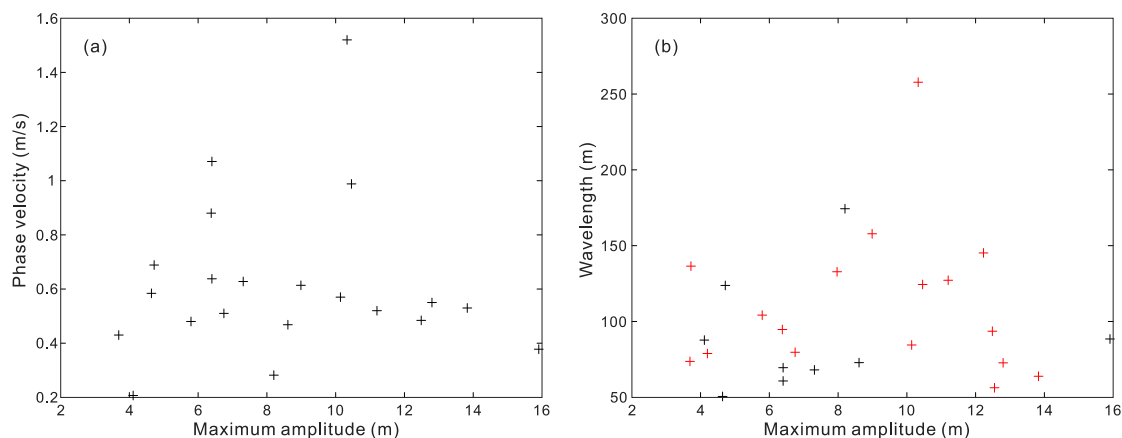
344 **Figure 9. (a) The relationship between the phase velocity and the maximum amplitude of the mode-2 ISWs observed in the study**
345 **area. (b) The relationship between the wavelength and the maximum amplitude of the mode-2 ISWs observed in the study area,**
346 **where the black and red crosses denote the ISWs on the survey lines in SW-NE direction and in NE-SW direction, respectively.**

347
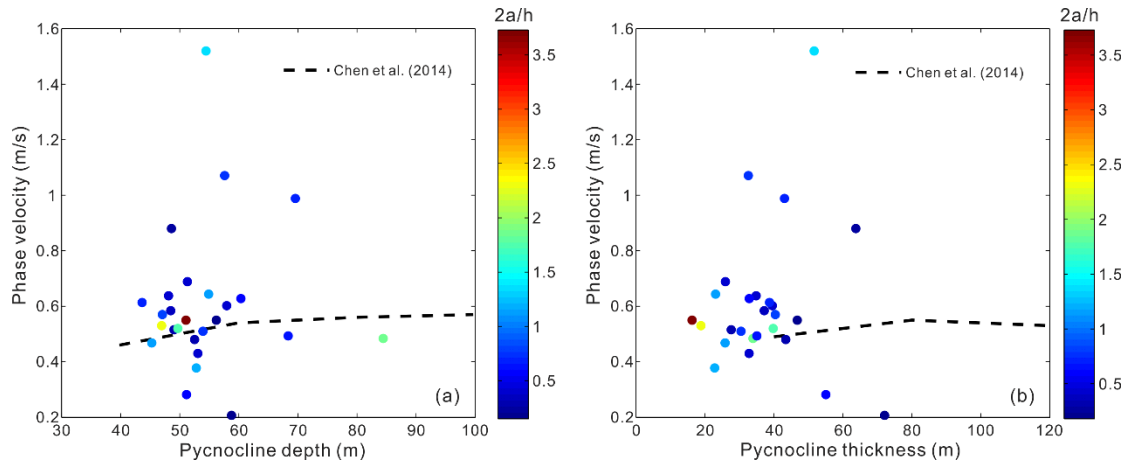
Figure 10. (a) The relationship between the phase velocity and the pycnocline depth of the mode-2 ISWs observed in the study area, (b) The relationship between the phase velocity and the pycnocline thickness of the mode-2 ISWs observed in the study area, the colour filled the circle indicates the dimensionless amplitude.

3.3 Vertical Structure Characteristics of the Mode-2 ISWs' Amplitude in Study Area

Observing the vertical structure of the mode-2 ISWs' amplitude in the study area, it is found that they follow the following characteristics as a whole. The amplitude of ISWs in the upper half of the pycnocline decreases with the increasing seawater depth. The amplitude of ISWs in the lower half of the pycnocline firstly increases and then decreases with the increasing seawater depth (see Figs. 11 and 12 in this paper, Fig. 5 of Fan et al., 2021a, and Fig. 6 of Fan et al., 2021b). Due to the influence of the pycnocline centre deviation on the development of the vertical structure of the ISWs' amplitude, the vertical structure of the mode-2 ISWs' amplitude in the study area generally only exhibits part of the characteristics given by the vertical mode function (the amplitude of the ISWs in the upper and lower half of the pycnocline firstly increases and then decreases with the increasing seawater depth, respectively, as shown by the blue and red curves in Figs. 11 and 12). Since the pycnocline centre of most of the mode-2 ISWs observed in the study area deviates upwards, the ISWs structure at the top is not as well developed as the ISWs structure at the bottom. Therefore, the amplitude of ISWs in the upper half of the pycnocline usually decreases with the increasing seawater depth. Figure 11 shows the vertical structure of the amplitude of the 10 mode-2 ISWs ISW1-ISW10 in the survey line L84. The pycnocline centres corresponding to ISW1-ISW7 all deviate upwards (see the degree to which the mid-depth of the pycnocline deviates from 1/2 seafloor depth in Table 1, the positive sign indicates that the pycnocline deviates upward, and the negative sign indicates that the pycnocline deviates downward), Among them, ISW1-ISW4 (Fig. 11a-d) and ISW7 (Fig. 11g) were only picked up one reflection event in upper half of the pycnocline. From ISW6 (Fig. 11f), it can be seen that the amplitude of ISWs in the upper half of the pycnocline decreases with the increasing seawater depth. From ISW2 (Fig. 11b), ISW4 (Fig. 11d), ISW5 (Fig. 11e), and ISW7 (Fig. 11g), it can be clearly seen that the amplitude of ISWs in the lower half of the pycnocline firstly increases and then decreases with the

372   increasing seawater depth. The pycnocline centres corresponding to ISW8-ISW10 all slightly deviate downwards (see the

373   degree to which the mid-depth of the pycnocline deviates from 1/2 seafloor depth in Table 1, the positive sign indicates that

374   the pycnocline deviates upward, and the negative sign indicates that the pycnocline deviates downward). From ISW8 (Fig.

375   11h) and ISW10 (Fig. 11j), it can be seen that the amplitude of ISWs in the upper half of the pycnocline decreases with the

376   increasing seawater depth. Figure 12 shows the vertical structure of the amplitude of the four mode-2 ISWs (ISW11, ISW12,

377   ISW16, and ISW17) in the survey line L74. The pycnocline centres corresponding to ISW11, ISW12, ISW16, and ISW17

378   significantly deviate downwards (see the degree to which the mid-depth of the pycnocline deviates from 1/2 seafloor depth

379   in Table 2, the positive sign indicates that the pycnocline deviates upward, and the negative sign indicates that the

380   pycnocline deviates downward), which makes the ISWs structure at the top more developed. From ISW11, ISW12, and

381   ISW17 (Fig. 12a, b, d), it can be seen that the amplitude of the ISWs in the upper half of the pycnocline firstly increases and

382   then decreases with the increasing seawater depth.

383
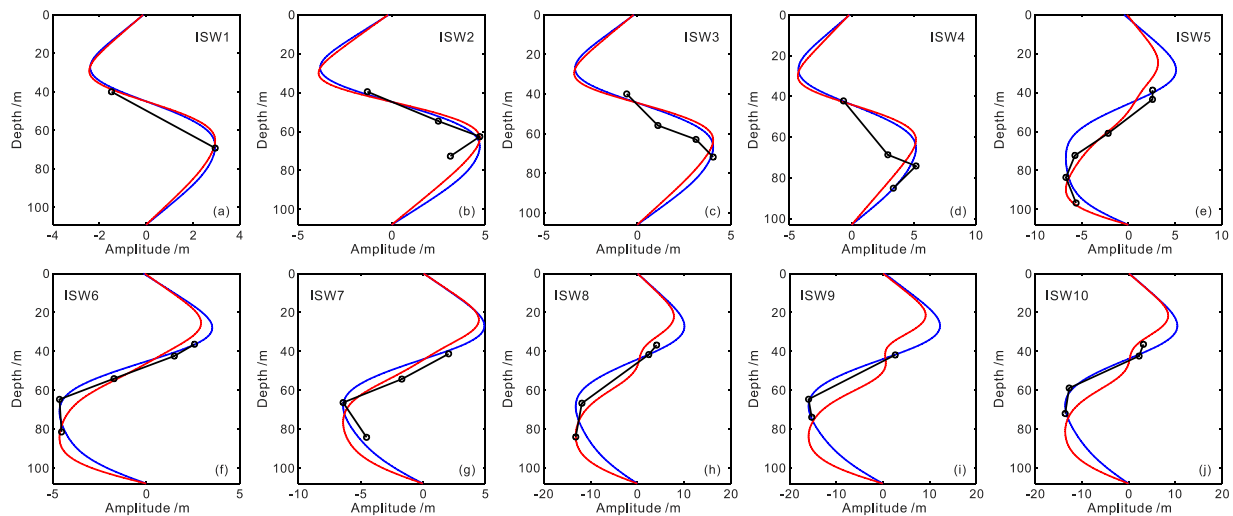
385   **Figure 11. (a)-(j) respectively demonstrate the vertical structure characteristics of the amplitude of the 10 mode-2 ISWs ISW1-**
386   **ISW10 in the survey line L84 as well as the vertical mode function fitting results. The black circles denote the observed ISWs'**
387   **amplitudes at different depths. The blue curves are the linear vertical mode function (nonlinear correction is not considered), and**
388   **the red curves are the first-order nonlinear vertical mode function (nonlinear correction is considered).**

389

390
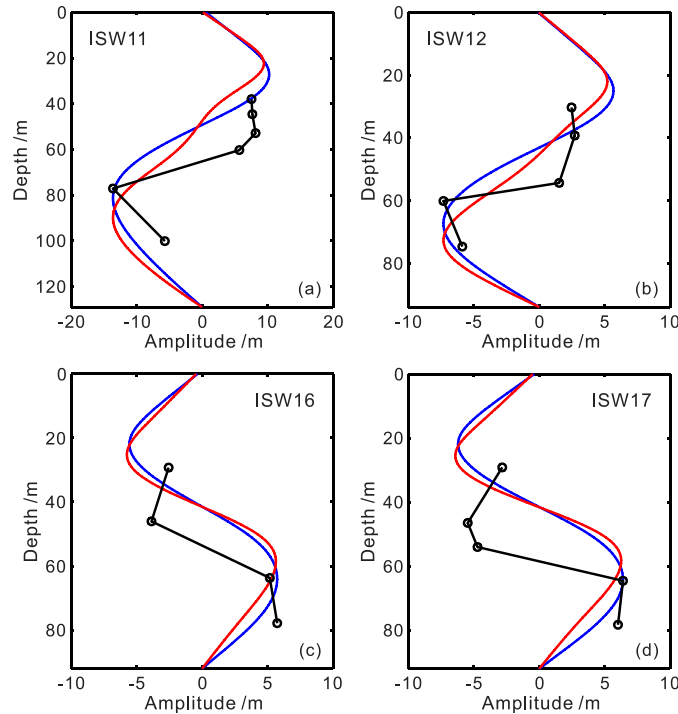
Figure 12. (a)-(d) respectively demonstrate the vertical structure characteristics of the amplitude of the four mode-2 ISWs (ISW11, ISW12, ISW16, and ISW17) in the survey line L74 as well as the vertical mode function fitting results. The black circles denote the observed ISWs' amplitudes at different depths. The blue curves are the linear vertical mode function (nonlinear correction is not considered), and the red curves are the first-order nonlinear vertical mode function (nonlinear correction is considered).

395

In order to study the vertical structure of the mode-2 ISWs' amplitude in more detailed for the study area, we respectively compare the observation result with the linear vertical mode function (nonlinear correction is not considered, the blue curves in Figs. 11 and 12) and the first-order nonlinear vertical mode function (considering nonlinear correction, the red curves in Figs. 11 and 12). The linear vertical mode function can be obtained by solving the eigenvalue equation that satisfies the Taylor-Goldstein problem (Holloway et al., 1999): $d^2\varphi(z)/dz^2+[N^2(z)-\omega^2]/C^2\varphi(z)=0$, $\varphi(0)=\varphi(-H)=0$. Where $\varphi(z)$ represents the linear vertical mode function, C is the linear phase velocity, $N(z)$ is the Brunt-Väisälä frequency, and ω is the wave frequency. The first-order nonlinear vertical mode function is obtained by adding a nonlinear correction term to the linear vertical mode function (Lamb and Yan, 1996), and it can be expressed by $\varphi_m(z)=\varphi(z)+\eta_0 T(z)$. Where η_0 is the ISWs maximum amplitude in the vertical direction, and $T(z)$ is the first-order nonlinear correction term. The detailed calculation process is described in Gong et al. (2021). Observing Fig. 11, it can be found that the overall nonlinearity of the ISWs ISW5 (Fig. 11e) and ISW8 (Fig. 11h) on the survey line L84 is relatively strong, and the first-order nonlinear vertical mode function considering nonlinear correction can be used to better fit the vertical structure of the amplitude (the red curves in Fig. 11e, h). The nonlinearity is relatively strong at the bottom of ISW2 (the seawater depth range is 60-80 m in Fig. 11b), the top of ISW7 (the seawater depth range is 40-60 m in Fig. 11g), and the top of ISW10 (the seawater depth is about 40 m

410   in Fig. 11j). And the first-order nonlinear vertical mode function considering nonlinear correction can be used to better fit the

411   vertical structure of the amplitude (the red curves in Fig. 11b, g, j). The overall nonlinearity of ISW1 (Fig. 11a), ISW3 (Fig.

412   11c), ISW6 (Fig. 11f), and ISW9 (Fig. 11i) is relatively weak, and the linear vertical mode function can be used to better fit

413   the vertical structure of the amplitude. The nonlinearity is relatively weak at the top of ISW2 (the seawater depth range is 40-

414   60 m in Fig. 11b), the bottom of ISW7 (the seawater depth range is 60-90 m in Fig. 11g), and the bottom of ISW10 (the

415   seawater depth is below 40 m in Fig. 11j). The linear vertical mode function can be used to better fit the vertical structure of

416   the amplitude (the blue curves in Fig. 11b, g, j). The above analysis reflects that the vertical structure of the mode-2 ISWs'

417   amplitude in the study area is affected by the nonlinearity degree of the ISWs. Observing Fig. 12, it can be found that neither

418   the linear vertical mode function (without considering nonlinear correction) nor the first-order nonlinear vertical mode

419   function (with consideration of nonlinear correction) can be used to well fit the vertical structure of the amplitude of the

420   ISWs ISW11, ISW12, ISW16, and ISW17 on L74 (especially the position of the upper half of the pycnocline). The ISWs

421   ISW11, ISW12, ISW16, and ISW17 on the survey line L74 have the large downward deviation of the pycnocline centre (see

422   the degree to which the mid-depth of the pycnocline deviates from 1/2 seafloor depth in Table 2, the positive sign indicates

423   that the pycnocline deviates upward, and the negative sign indicates that the pycnocline deviates downward). We observed

424   the fitting result of the vertical amplitude of the ISWs with the large downward pycnocline deviation on other lines of the

425   study area (not shown in this article), and found that the fitting result of the vertical amplitude is usually poorer than that of

426   the ISWs corresponding to the upward deviation of the pycnocline (especially the position of the upper half of the

427   pycnocline). We believe that when the pycnocline centre has the large downward deviation, the vertical mode function

428   (including the linear vertical mode function without considering nonlinear correction and the first-order nonlinear vertical

429   mode function considering nonlinear correction) cannot be used to well fit the vertical structure of the mode-2 ISWs'

430   amplitude in the study area. The above analysis once again reflects that the pycnocline deviation (especially the downward

431   deviation of the pycnocline) affects the vertical structure of the mode-2 ISWs' amplitude in the study area.

432   **4 Discussion**

433   As for the relationship between the dimensionless phase velocity and the dimensionless amplitude of the mode-2 ISWs

434   in the study area, as well as the relationship between the dimensionless wavelength and the dimensionless amplitude, both of

435   them are not strictly monotonous in the case of smaller amplitude ($2a/h_2<1$) and show the characteristics of multi-parameter

436   controlling. For this reason, we analysed the influence of seawater depth on the dimensionless phase velocity and

437   dimensionless wavelength of the mode-2 ISWs in the study area. The results are shown in Fig. 13a and b, respectively.

438   Observing Fig. 13a, it can be found that in the shallow seawater (the seafloor depth is less than 120 m) the dimensionless

439   phase velocity variation range is small, and there are both the large-amplitude mode-2 ISWs ($2a/h_2>2$) and the small-

440   amplitude mode-2 ISWs ($2a/h_2<2$). In the deep seawater (or at the shelf break, the seafloor depth is greater than 120m), the

441   smaller-amplitude mode-2 ISWs ($2a/h_2<1$, dark blue filled circles in Fig. 13a) have a large dimensionless phase velocity

442   variation range. The maximum dimensionless phase velocity can reach 2.45, and the minimum can reach 0.5. In particular,

443   the smaller dimensionless phase velocities are mainly concentrated in the deep seawater, so that in Fig. 7 when $2a/h_2<1$ the

444   relationship between the dimensionless phase velocity and the dimensionless amplitude of the mode-2 ISWs has the trend

445   given by Kozlov and Makarov (1990). The sharp decrease in the dimensionless phase velocities of the mode-2 ISWs with

446   smaller amplitudes in the deep seawater may be caused by the collision of the ISWs with the seafloor topography (including

447   the step) at the shelf break. In addition, from Fig. 10a and b, it can be found that on the whole, the pycnocline depth and the

448   pycnocline thickness of the larger-amplitude mode-2 ISWs ($2a/h_2>1$) are respectively smaller than the pycnocline depth and

449   the pycnocline thickness of the smaller-amplitude mode-2 ISWs ($2a/h_2<1$). Therefore, the phase velocities of the larger-

450   amplitude mode-2 ISWs ($2a/h_2>1$) are generally smaller than the phase velocities of the smaller-amplitude mode-2 ISWs

451   ($2a/h_2<1$). In Fig. 7 when $2a/h_2>1$, this makes the relationship between the dimensionless phase velocity and the

452   dimensionless amplitude of the mode-2 ISWs is closer to the result predicted by the deep water weakly nonlinear theory

453   (Benjamin, 1967). The above-analysed influences of the seawater depth (seafloor topography), the pycnocline depth and the

454   pycnocline thickness on the mode-2 ISWs phase velocity of the study area have caused the diversity of the relationship

455   between dimensionless phase velocity and dimensionless amplitude. That is, when $2a/h_2<1$, the relationship between the

456   dimensionless phase velocity and the dimensionless amplitude of the observed mode-2 ISWs in the study area has the trends

457   respectively given by Kozlov and Makarov (1990), as well as Salloum et al. (2012). when $2a/h_2>1$, the relationship between

458   the dimensionless phase velocity and the dimensionless amplitude of the observed mode-2 ISWs in the study area is closer to

459   the result predicted by the deep water weakly nonlinear theory (Benjamin, 1967).

460   Observing Fig. 13b, it can be found that the mode-2 ISWs with the smaller amplitudes ($2a/h_2<1$, the dark blue filled

461   circles in Fig. 13b) have a relatively large variation range of the dimensionless wavelength in the deep seawater (the seafloor

462   depth is greater than 120m). The largest dimensionless wavelength can reach up to 9.55 (corresponding to ISW2 on the

463   survey line L84, whose pycnocline deviation is large and waveform is asymmetric), and the smallest dimensionless

464   wavelength can reach 2.44, so that the dimensionless wavelength of the vertical axis in Fig. 8 can be reduced to 2.44 when

465   $2a/h_2<1$. The sharp decrease in the dimensionless wavelengths of the mode-2 ISWs with the smaller amplitudes ($2a/h_2<1$) in

466   deep seawater may be caused by the collision of the ISWs with the seafloor topography at the shelf break. The sharp increase

467   in dimensionless wavelengths of the mode-2 ISWs with the smaller amplitudes in deep seawater may be related to the

468   waveform asymmetry caused by the pycnocline deviation.

469

470
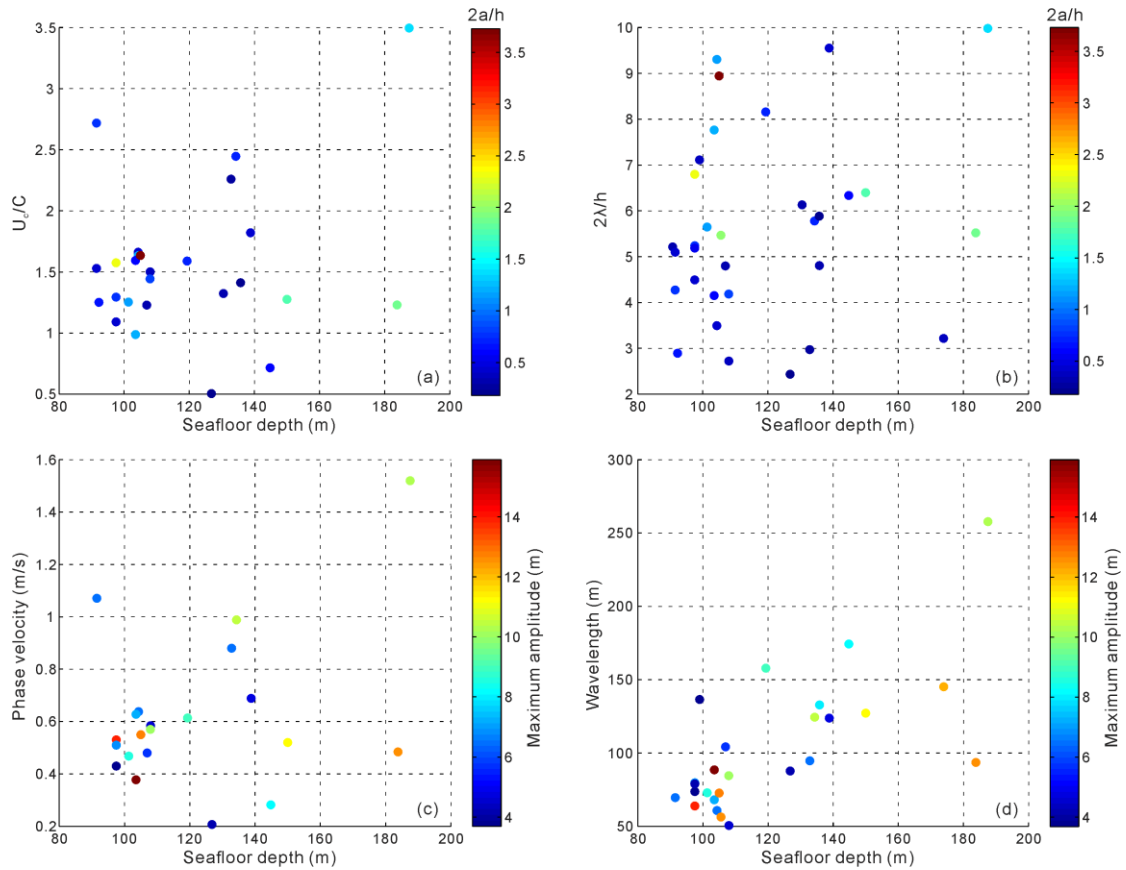
Figure 13. (a) the relationship between the dimensionless phase velocity and the seawater depth of the mode-2 ISWs observed in the study area, the colour of the filled circle indicates the dimensionless amplitude. (b) The relationship between the dimensionless wavelength and the seawater depth of the mode-2 ISWs observed in the study area, the colour of the filled circle indicates the dimensionless amplitude. (c) The relationship between the phase velocity and the seawater depth of the mode-2 ISWs observed in the study area, the colour of the filled circle indicates the maximum amplitude. (d) The relationship between the wavelength and the seawater depth of the mode-2 ISWs observed in the study area, the colour of the filled circle indicates the maximum amplitude.

477

478   Fig. 13c and d respectively show the relationship between the phase velocity and the seawater depth, and the

479 relationship between the wavelength and the seawater depth of the mode-2 ISWs in the study area. The colour of the filled

480 circles in the figures represents the maximum amplitude. Observing Fig. 13c, it can be found that the seawater depth in the

481 study area has the great influence on the phase velocity of the mode-2 ISWs. In the shallow seawater area (the seawater

482 depth is less than 120 m), the phase velocity variety range is small. In the deep seawater area (the seawater depth is larger

483 than 120 m) the phase velocity has the large variety range. The maximum phase velocity is 1.52 m/s and the minimum phase

484 velocity is 0.21 m/s. In Fig. 9a, when the maximum amplitude is between 6 m and 11 m, the phase velocity has the larger

485 variety range, and there is the significant increase in the phase velocity. The above phenomenon is controlled by the seawater

486 depth. That is, in the deep seawater area (seawater depth greater than 120 m), for the ISWs with the maximum amplitude of

487 6-11 m, the phase velocity varies widely, and the maximum phase velocity of 1.52 m/s appears (Fig. 13c). Observing Fig.

488   13d, it can be found that the seawater depth in the study area has the great influence on the wavelength of the mode-2 ISWs.

489   On the whole, the wavelength of the ISWs increases with the increasing seawater depth. For the ISWs with the maximum

490   amplitude of 7-13 m, a considerable part of them are distributed in the deep seawater area (the seawater depth is larger than

491   120 m), making their wavelengths increase significantly. As a result, when the maximum amplitude is between 7 m and 13

492   m in Fig. 9b, there is the significant increase in the wavelength.

5 Conclusions

494   A regional study of the mode-2 ISWs in the Pacific coast of Central America was carried out by using seismic reflection.

495   Through the analysis of the typical seismic sections L84 and L74, it is found that when the degree of downward pycnocline

496   deviation is large, the influence of pycnocline deviation on the stability of the mode-2 ISWs is more complicated than when

497   the pycnocline deviates upwards. There are mode-2 ISWs with the large degree of downward pycnocline deviation but with

498   the relatively symmetrical waveform.

499   The observed relationship between the dimensionless phase velocity U_c/C and the dimensionless amplitude $2a/h_2$ of the

500   mode-2 ISWs in the study area was analysed. When $2a/h_2<1$, U_c/C increases with the increasing $2a/h_2$, divided into two parts

501   with different growth rates. When $2a/h_2>1$, U_c/C increases with the increasing $2a/h_2$ at a relatively small growth rate. The

502   observed relationship between the dimensionless wavelength $2\lambda/h_2$ and the dimensionless amplitude $2a/h_2$ of the mode-2

503   ISWs in the study area was also analysed. When $2a/h_2<1$, $2\lambda/h_2$ decreases with the increasing $2a/h_2$. When $2a/h_2>2$, $2\lambda/h_2$

504   increases with the increasing $2a/h_2$. As for the relationships between U_c/C and $2a/h_2$, as well as $2\lambda/h_2$ and $2a/h_2$ of the mode-2

505   ISWs in the study area, both of them show the characteristics of multi-parameter controlling. The influences of the seawater

506   depth (seafloor topography), the pycnocline depth, and the pycnocline thickness on the mode-2 ISWs phase velocity of the

507   study area have caused the diversity of the relationship between U_c/C and $2a/h_2$.

508   The vertical structure of the mode-2 ISWs' amplitude in the study area is affected by the nonlinearity degree of the

509   ISWs. Part of the mode-2 ISWs with the strong nonlinearity (or the part with strong nonlinearity of the ISWs in the vertical

510   direction) can use the first-order nonlinear vertical mode function (nonlinear correction is considered) to better fit the vertical

511   structure of the amplitude. The pycnocline deviation (especially the downward deviation of the pycnocline) affects the

512   vertical structure of the mode-2 ISWs' amplitude in the study area. When the pycnocline centre has the large downward

513   deviation, the vertical mode function cannot be used to well fit the vertical structure of the mode-2 ISWs' amplitude in the

514   study area.

515 **Code and data availability.** The full seismic data are provided by MGDS (The Marine Geoscience Data System)
516 (http://www.marine-geo.org/), available for academic research at www.marine-geo.org/tools/search/entry.php?id=EW0412.
517 The temperature and salinity data comes from CMEMS (Copernicus Marine Environment Monitoring Service)
518 (http://marine.copernicus.en/ services- portfolio/access-to-products/).

519 **Author contribution.** The concept of this study was developed by Haibin Song and extended upon by all involved. Wenhao
520 Fan implemented the study and performed the analysis with guidance from Haibin Song. Yi Gong, Shun Yang and Kun
521 Zhang collaborated in discussing the results and composing the manuscript.

522 **Competing interests.** The authors declare that they have no conflict of interest.

523 **Acknowledgements.** We thank the captain, crew, and science party of R/V Maurice Ewing cruise EW0412 for acquiring the
524 seismic data. We appreciate MGDS and CMEMS for their supporting data used in this study. This work is supported by the
525 National Natural Science Foundation of China (Grant Number 41976048) and the National Key R&D Program of China
526 (2018YFC0310000).

527 **References**

528 Bai, Y., Song, H., Guan, Y., and Yang, S.: Estimating depth of polarity conversion of shoaling internal solitary waves in the
529   northeastern South China Sea, Continental Shelf Research, 143, 9-17, https://doi.org/10.1016/j.csr.2017.05.014, 2017.

530 Benjamin, T. B.: Internal waves of permanent form in fluids of great depth, Journal of Fluid Mechanics, 29, 559-592,
531   https://doi.org/10.1017/S002211206700103X, 1967.

532 Biescas, B., Armi, L., Sallarès, V., and Gràcia, E.: Seismic imaging of staircase layers below the Mediterranean
533   Undercurrent, Deep Sea Research Part I: Oceanographic Research Papers, 57, 1345–1353,
534   https://doi.org/10.1016/j.dsr.2010.07.001, 2010.

535 Biescas, B., Sallarès, V., Pelegrí, J. L., Machín, F., Carbonell, R., Buffett, G., Dañobeitia, J.J., and Calahorrano, A.: Imaging
536   meddy finestructure using multichannel seismic reflection data, Geophysical Research Letters, 35, L11609,
537   https://doi.org/10.1029/2008GL033971, 2008.

538 Bogucki, D. J., Redekopp, L. G., and Barth, J.: Internal solitary waves in the Coastal Mixing and Optics 1996 experiment:
539   Multimodal structure and resuspension, Journal of Geophysical Research: Oceans, 110,
540   https://doi.org/10.1029/2003JC002253, 2005.

541 Brandt, A., and Shipley, K. R.: Laboratory experiments on mass transport by large amplitude mode-2 internal solitary waves,
542   Physics of Fluids, 26, 046601, https://doi.org/10.1063/1.4869101, 2014.

543 Carr, M., Davies, P. A., and Hoebers, R. P.: Experiments on the structure and stability of mode-2 internal solitary-like waves
544   propagating on an offset pycnocline, Physics of Fluids, 27, 046602, https://doi.org/10.1063/1.4916881, 2015.

545   Chen, Z. W., Xie, J., Wang, D., Zhan, J. M., Xu, J., and Cai, S.: Density stratification influences on generation of different
546   modes internal solitary waves, Journal of Geophysical Research: Oceans, 119, 7029-7046,
547   https://doi.org/10.1002/2014JC010069, 2014.

548   Cheng, M. H., Hsieh, C. M., Hwang, R. R., and Hsu, J. R. C.: Effects of initial amplitude and pycnocline thickness on the
549   evolution of mode-2 internal solitary waves, Physics of Fluids, 30, 042101, https://doi.org/10.1063/1.5020093, 2018.

550   Da Silva, J. C. B., New, A. L., and Magalhaes, J. M.: On the structure and propagation of internal solitary waves generated at
551   the Mascarene Plateau in the Indian Ocean, Deep Sea Research Part I: Oceanographic Research Papers, 58, 229-240,
552   https://doi.org/10.1016/j.dsr.2010.12.003, 2011.

553   Deepwell, D., Stastna, M., Carr, M., and Davies, P. A.: Wave generation through the interaction of a mode-2 internal solitary
554   wave and a broad, isolated ridge, Physical Review Fluids, 4, 094802, https://doi.org/10.1103/PhysRevFluids.4.094802,
555   2019.

556   Fan, W., Song, H., Gong, Y., Sun, S., Zhang, K., Wu, D., Kuang, Y., and Yang, S.: The shoaling mode-2 internal solitary
557   waves in the Pacific coast of Central America investigated by marine seismic survey data, Continental Shelf Research,
558   212, 104318, https://doi.org/10.1016/j.csr.2020.104318, 2021a.

559   Fan, W., Song, H., Gong, Y., Zhang, K., and Sun, S.: Seismic oceanography study of mode-2 internal solitary waves
560   offshore Central America, Chinese Journal of Geophysics-Chinese Edition, 64, 195-208,
561   https://doi.org/10.6038/cjg2021O0071, 2021b.

562   Fer, I., Nandi, P., Holbrook, W. S., Schmitt, R. W., and Páramo, P.: Seismic imaging of a thermohaline staircase in the
563   western tropical North Atlantic, Ocean Science, 6, 621–631, https://doi.org/10.5194/os-6-621-2010, 2010.

564   Fulthorpe, C., and McIntosh, K.: Raw Multi-Channel Seismic Shot Data from the Sandino Basin, offshore Nicaragua,
565   acquired during R/V Maurice Ewing expedition EW0412 (2004), Interdisciplinary Earth Data Alliance (IEDA) [data
566   set], https://doi.org/10.1594/IEDA/309938, 2014.

567   Geng, M., Song, H., Guan, Y., and Bai, Y.: Analyzing amplitudes of internal solitary waves in the northern South China Sea
568   by use of seismic oceanography data, Deep Sea Research Part I: Oceanographic Research Papers, 146, 1-10,
569   https://doi.org/0.1016/j.dsr.2019.02.005, 2019.

570   Gong, Y., Song, H., Zhao, Z., Guan, Y., and Kuang, Y.: On the vertical structure of internal solitary waves in the
571   northeastern South China Sea, Deep Sea Research Part I: Oceanographic Research Papers, 173, 103550,
572   https://doi.org/10.1016/j.dsr.2021.103550, 2021.

573   Holbrook, W. S., and Fer, I.: Ocean internal wave spectra inferred from seismic reflection transects, Geophysical Research
574   Letters, 32, L15604, https://doi.org/10.1029/2005GL023733, 2005.

575   Holbrook, W. S., Fer, I., Schmitt, R. W., Lizarralde, D., Klymak, J. M., Helfrich, L. C., and Kubichek, R.: Estimating
576   oceanic turbulence dissipation from seismic images, Journal of Atmospheric and Oceanic Technology, 30, 1767–1788,
577   https://doi.org/10.1175/JTECH-D-12-00140.1, 2013.

578   Holbrook, W. S., Páramo, P., Pearse, S., and Schmitt, R. W.: Thermohaline fine structure in an oceanographic front from
579   seismic reflection profiling, Science, 301, 821-824, https://doi.org/10.1126/science.1085116, 2003.

580   Holloway, P. E., Pelinovsky, E., and Talipova, T.: A generalized Korteweg-de Vries model of internal tide transformation in
581   the coastal zone, Journal of Geophysical Research: Oceans, 104, 18333-18350, https://doi.org/10.1029/1999JC900144,
582   1999.

583   Kozlov, V. F., and Makarov, V. G.: On a class of stationary gravity currents with the density jump, Izvestiâ Akademii nauk
584   SSSR. Fizika atmosfery i okeana, 26, 395-402, 1990.

585   Kurkina, O., Talipova, T., Soomere, T., Giniyatullin, A., and Kurkin, A.: Kinematic parameters of internal waves of the
586   second mode in the South China Sea, Nonlinear Processes in Geophysics, 24, 645-660, https://doi.org/10.5194/npg-24-
587   645-2017, 2017.

588   Lamb, K. G., and Yan, L.: The evolution of internal wave undular bores: comparisons of a fully nonlinear numerical model
589   with weakly nonlinear theory, Journal of physical oceanography, 26, 2712-2734, https://doi.org/10.1175/1520-
590   0485(1996)026<2712:TEOIWU>2.0.CO;2, 1996.

591   Liu, A. K., Su, F. C., Hsu, M. K., Kuo, N. J., and Ho, C. R.: Generation and evolution of mode-two internal waves in the
592   South China Sea, Continental Shelf Research, 59, 18-27, https://doi.org/10.1016/j.csr.2013.02.009, 2013.

593   Maderich, V., Jung, K. T., Terletska, K., Brovchenko, I., and Talipova, T.: Incomplete similarity of internal solitary waves
594   with trapped cores, Fluid Dynamics Research, 47, 035511, https://doi.org/10.1088/0169-5983/47/3/035511, 2015.

595   Maxworthy, T.: Experiments on solitary internal Kelvin waves, Journal of Fluid Mechanics, 129, 365-383,
596   https://doi.org/10.1017/S0022112083000816, 1983.

597   Olsthoorn, J., Baglaenko, A., and Stastna, M.: Analysis of asymmetries in propagating mode-2 waves, Nonlinear Processes
598   in Geophysics, 20, 59-69, https://doi.org/10.5194/npg-20-59-2013, 2013.

599   Pinheiro, L. M., Song, H., Ruddick, B., Dubert, J., Ambar, I., Mustafa, K., and Bezerra, R.: Detailed 2-D imaging of the
600   Mediterranean outflow and meddies off W Iberia from multichannel seismic data, Journal of Marine Systems, 79, 89–
601   100, https://doi.org/10.1016/j.jmarsys.2009.07.004, 2010.

602   Ramp, S. R., Yang, Y. J., Reeder, D. B., Buijsman, M. C., and Bahr, F. L.: The evolution of mode-2 nonlinear internal waves
603   over the northern Heng-Chun Ridge south of Taiwan, Nonlinear Processes in Geophysics, 22, 413-431,
604   https://doi.org/10.5194/npg-22-413-2015, 2015.

605   Rayson, M. D., Jones, N. L., and Ivey, G. N.: Observations of large-amplitude mode-2 nonlinear internal waves on the
606   Australian North West shelf, Journal of Physical Oceanography, 49, 309-328, https://doi.org/10.1175/JPO-D-18-0097.1,
607   2019.

608   Ruddick, B., Song, H. B., Dong, C., and Pinheiro, L.: Water column seismic images as maps of temperature gradient,
609   Oceanography, 22, 192–205, https://doi.org/10.5670/oceanog.2009.19, 2009.

610 Sallares, V., Mojica, J. F., Biescas, B., Klaeschen, D., and Gràcia, E.: Characterization of the sub-mesoscale energy cascade
611   in the Alboran Sea thermocline from spectral analysis of high-resolution MCS data, Geophysical Research Letters, 43,
612   6461–6468, https://doi.org/10.1002/2016GL069782, 2016.

613 Salloum, M., Knio, O. M., and Brandt, A.: Numerical simulation of mass transport in internal solitary waves, Physics of
614   Fluids, 24, 016602, https://doi.org/10.1063/1.3676771, 2012.

615 Sheen, K. L., White, N. J., and Hobbs, R. W.: Estimating mixing rates from seismic images of oceanic structure,
616   Geophysical Research Letters, 36, L00D04, https://doi.org/10.1029/2009GL040106, 2009.

617 Shroyer, E. L., Moum, J. N., and Nash, J. D.: Mode 2 waves on the continental shelf: Ephemeral components of the
618   nonlinear internal wavefield, Journal of Geophysical Research: Oceans, 115, https://doi.org/10.1029/2009JC005605,
619   2010.

620 Stamp, A. P., and Jacka, M.: Deep-water internal solitaty waves, Journal of Fluid Mechanics, 305, 347-371,
621   https://doi.org/10.1017/S0022112095004654, 1995.

622 Sun, S. Q., Zhang, K., and Song, H. B.: Geophysical characteristics of internal solitary waves near the Strait of Gibraltar in
623   the Mediterranean Sea, Chinese Journal of Geophysics-Chinese Edition, 62, 2622–2632,
624   https://doi.org/10.6038/cjg2019N0079, 2019.

625 Tang, Q., Wang, C., Wang, D., and Pawlowicz, R.: Seismic, satellite, and site observations of internal solitary waves in the
626   NE South China Sea, Scientific Reports, 4, 5374, https://doi.org/10.1038/srep05374, 2014.

627 Tang, Q., Xu, M., Zheng, C., Xu, X., and Xu, J.: A locally generated high-mode nonlinear internal wave detected on the
628   shelf of the northern South China Sea from marine seismic observations, Journal of Geophysical Research: Oceans, 123,
629   1142–1155, https://doi.org/10.1002/2017JC013347, 2018.

630 Terez, D. E., and Knio, O. M.: Numerical simulations of large-amplitude internal solitary waves, Journal of Fluid Mechanics,
631   362, 53-82, https://doi.org/10.1017/S0022112098008799, 1998.

632 Terletska, K., Jung, K. T., Talipova, T., Maderich, V., Brovchenko, I., and Grimshaw, R.: Internal breather-like wave
633   generation by the second mode solitary wave interaction with a step, Physics of Fluids, 28, 116602,
634   https://doi.org/10.1063/1.4967203, 2016.

635 Tsuji, T., Noguchi, T., Niino, H., Matsuoka, T., Nakamura, Y., Tokuyama, H., Kuramoto, S.I. and Bangs, N.: Two-
636   dimensional mapping of fine structures in the Kuroshio Current using seismic reflection data, Geophysical Research
637   Letters, 32, L14609, https://doi.org/10.1029/2005GL023095, 2005.

638 Yang, Y.J., Fang, Y.C., Chang, M.H., Ramp, S.R., Kao, C.C., and Tang, T.Y.: Observations of second baroclinic mode
639   internal solitary waves on the continental slope of the northern South China Sea, Journal of Geophysical Research:
640   Oceans, 114, https://doi.org/10.1029/2009JC005318, 2009.